Estimation of microtubule-generated forces using a DNA origami nanospring

Nick Maleki, Ali; Huis In 't Veld, Pim J.; Akhmanova, Anna; Dogterom, Marileen; Volkov, Vladimir A.

DOI
10.1242/jcs.260154

Publication date
2023

Document Version
Final published version

Published in
Journal of cell science

© 2022. Published by The Company of Biologists Ltd | Journal of Cell Science (2023) 136, jcs260154. doi:10.1242/jcs.260154

TOOLS AND RESOURCES

SPECIAL ISSUE: CELL BIOLOGY OF MOTORS

Estimation of microtubule-generated forces using a DNA origami nanospring

Ali Nick Maleki[1], Pim J. Huis in 't Veld[2], Anna Akhmanova[3], Marileen Dogterom[1] and Vladimir A. Volkov[1,4,*]

ABSTRACT

Microtubules are dynamic cytoskeletal filaments that can generate forces when polymerizing and depolymerizing. Proteins that follow growing or shortening microtubule ends and couple forces to cargo movement are important for a wide range of cellular processes. Quantifying these forces and the composition of protein complexes at dynamic microtubule ends is challenging and requires sophisticated instrumentation. Here, we present an experimental approach to estimate microtubule-generated forces through the extension of a fluorescent spring-shaped DNA origami molecule. Optical readout of the spring extension enables recording of force production simultaneously with single-molecule fluorescence of proteins getting recruited to the site of force generation. DNA nanosprings enable multiplexing of force measurements and only require a fluorescence microscope and basic laboratory equipment. We validate the performance of DNA nanosprings against results obtained using optical trapping. Finally, we demonstrate the use of the nanospring to study proteins that couple microtubule growth and shortening to force generation.

KEY WORDS: DNA origami, Force sensor, Microtubule, Dynein, Kinetochore, Optical trap

INTRODUCTION

Microtubules are dynamic polymers that can exert pushing and pulling forces when they grow and shorten. Microtubule-generated forces are important at various stages of the cell cycle in a variety of cell types and contexts (reviewed in Gudimchuk and McIntosh, 2021). One of the most well-studied processes relying on microtubule-generated forces is mitotic cell division, when the ends of microtubules pull on the centromeric regions of chromosomes through protein structures called kinetochores (Musacchio and Desai, 2017). The microtubule–kinetochore interface is force sensitive – tension at the centromere is thought to be converted into a biochemical signal that silences the mitotic checkpoint. However, the nature of the force sensor that responds to the microtubule-generated tension in the kinetochore is still unclear (reviewed in Audett and Maresca, 2020).

Precise measurements of microtubule-generated forces and responses to these forces are challenging *in vivo*, because of crowded cellular environments, a multitude of differently directed forces that are exerted by different cellular components, and difficulties in incorporating force-measuring equipment into the cell. The method of choice for precision force measurements has been *in vitro* reconstitution and optical trapping. An optical trap holds a plastic or glass sphere (bead) in the centre of a tightly focused infrared laser beam. Bead displacement from the beam can be monitored with nanometre precision using sophisticated optical equipment (Nicholas et al., 2014; Baclayon et al., 2017). Forces measured using beads coated with microtubule-binding proteins or purified kinetochore particles have provided important insights into the action of a microtubule as a motor (Grishchuk et al., 2005), the force-dependent stabilization of the kinetochore–microtubule interface (Akiyoshi et al., 2010; Miller et al., 2016), and molecular determinants of kinetochore-mediated stabilization of microtubule ends (Volkov et al., 2018; Huis in 't Veld et al., 2019).

Although having outstanding force and time resolution, the optical trapping approaches present several challenges. First, building an optical trap requires optical and engineering expertise, and commercial systems are expensive. Second, the trap acts on the centre of a bead, while force-generating biomolecules act on the surface of the bead, which can create asymmetry of the applied force in the bead–microtubule system (Volkov et al., 2013; Pyrpassopoulos et al., 2020). Finally, to study effects of force on dynamics of microtubule-binding or kinetochore proteins, one has to record these dynamics simultaneously with force. Addition of single-molecule fluorescence imaging to an optical trap is technically demanding (Lang et al., 2004; Lee et al., 2007; Deng and Asbury, 2017) and not widely accessible.

Here, we present a method to simultaneously measure microtubule-generated forces and single-molecule fluorescence intensities *in vitro* without an optical trap. The method is based on a previously described DNA origami spring-shaped structure, designed to determine forces directly from its extension (Iwaki et al., 2016). The nanospring is assembled by folding a long single-stranded DNA with short DNA oligonucleotides (staples), resulting in a spring-shaped bundle of four DNA strands (Fig. 1A; Iwaki et al., 2016). We provide detailed instructions to modify the original spring design, purify the DNA nanosprings, and use them as sensors for forces produced by growing and shortening microtubules.

We provide typical results in three different *in vitro* systems. First, we validate the nanospring-based estimation of force against optical trapping by measuring the stall force of dynein motors walking along the stabilized microtubules. We then demonstrate the use of the nanosprings to measure the forces generated by dynamic microtubules. Focusing on forces produced by microtubule growth, we reconstitute the forces exerted through an EB3 (encoded by *MAPRE3*) comet following the growing microtubule ends and pulling on nanospring-bound cargo containing an EB-binding SxIP

[1]Department of Bionanoscience, Kavli Institute of Nanoscience, Delft University of Technology, Delft 2629 HZ, The Netherlands. [2]Department of Mechanistic Cell Biology, Max Planck Institute of Molecular Physiology, Dortmund 44227, Germany. [3]Cell Biology, Neurobiology and Biophysics, Department of Biology, Faculty of Science, Utrecht University, Utrecht 3584 CH, The Netherlands. [4]School of Biological and Behavioural Sciences, Queen Mary University of London, London E1 4NS, UK.

*Author for correspondence (v.volkov@qmul.ac.uk)

P.J.H., 0000-0003-0234-6390; A.A., 0000-0002-9048-8614; M.D., 0000-0002-8803-5261; V.A.V., 0000-0002-5407-3366

Handling Editor: Anne Straube
Received 21 April 2022; Accepted 26 August 2022

Journal of Cell Science

Journal of Cell Science (2023) 136, jcs260154. doi:10.1242/jcs.260154

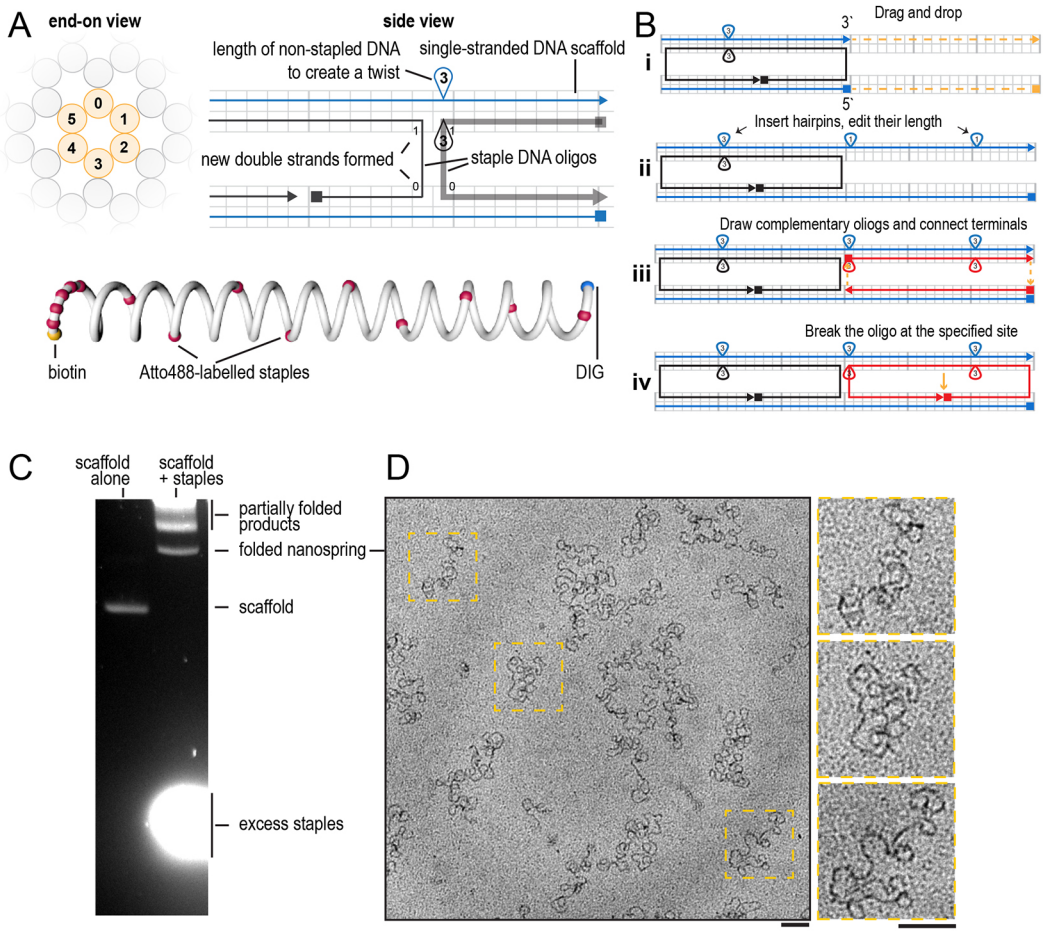

Fig. 1. Nanospring representation in caDNAno and quality control of folded nanospring by agarose gel electrophoresis and electron microscopy. (A) An example of a slice panel (left) and a path panel (right) of the DNA origami design in caDNAno. Below: a schematic illustration of the nanospring with colour-coded staples (yellow, biotin; red, fluorescently labelled staples; blue, DIG). (B) Step by step visual guide to extend an existing nanospring design using caDNAno. (C) Purification of nanosprings by agarose gel electrophoresis. The left lane shows migration of unfolded scaffold in absence of staples, the right lane is loaded with staple-scaffold mixture after temperature cycling and contains the products of folding. (D) Transmission electron microscopy of nanosprings negatively stained by 2% uranyl acetate. Enlarged images of the indicated regions are shown on the right. Scale bars: 100 nm. Images in C and D are representative of 11 experiments.

motif. Finally, we focus on forces produced by shortening microtubule ends in the context of kinetochore–microtubule interactions. We attach human kinetochore complex Ndc80 to the nanospring, and monitor spring extension simultaneously with the binding and unbinding of the spindle and kinetochore-associated (Ska) complex, another microtubule-binding kinetochore component. Using the DNA origami nanospring, we demonstrate that the presence of additional copies of Ndc80, but not Ska, increases the amount of force that shortening microtubule ends transmit to their cargo.

RESULTS

Design and calibration of the nanosprings

To make the DNA nanospring, we adapted the reported DNA origami design (Iwaki et al., 2016) to other single-stranded DNA scaffolds (see Materials and Methods for a detailed protocol). The spring was assembled into a four-stranded DNA bundle with a three nucleotide-long hairpin inserted at every 14 bp, creating an offset to twist the spring (Fig. 1A). Digoxigenin (DIG)- and biotin-labelled DNA staples were introduced at the termini of the spring for attachment to the molecules of interest. Further, nine Atto488-labelled staple oligonucleotides were evenly distributed along the length of the spring, and another five Atto488-labelled oligonucleotides added next to the biotin-labelled end (Fig. 1A). Spring design can be easily modified using caDNAno software (Fig. 1B; https://cadnano.org/) (Douglas et al., 2009). Folded springs need to be separated from the short staple oligonucleotides and partially folded products (Fig. 1C). We validated the purity and folding of our DNA nanosprings using negative stain electron microscopy (EM) (Fig. 1D).

To calibrate the force–extension profile of the springs, we attached the springs to the hydrophobic silanized glass surface of a flow chamber using anti-DIG IgG (Fig. 2A). Following a passivation step using Pluronic F-127, we obtained a uniform coating of single fluorescently labelled springs on the coverslip (Fig. 2B). We then used 1 µm streptavidin-coated beads bound to the springs via biotin–streptavidin linkage (Fig. 2C). Upon trapping a bead that was bound to the coverslip via the nanospring, displacement of the bead from the trap was measured as the flow chamber was moved using a piezo-driven stage in 100 nm steps, following a 2D matrix (Fig. 2D). After radial averaging of the force–extension data for six beads and accounting for the bead radius, the resulting force–extension curve was identical to that previously published (Iwaki et al., 2016). Fitting the data to an exponential growth equation produced the following relationship,

Journal of Cell Science (2023) 136, jcs260154. doi:10.1242/jcs.260154

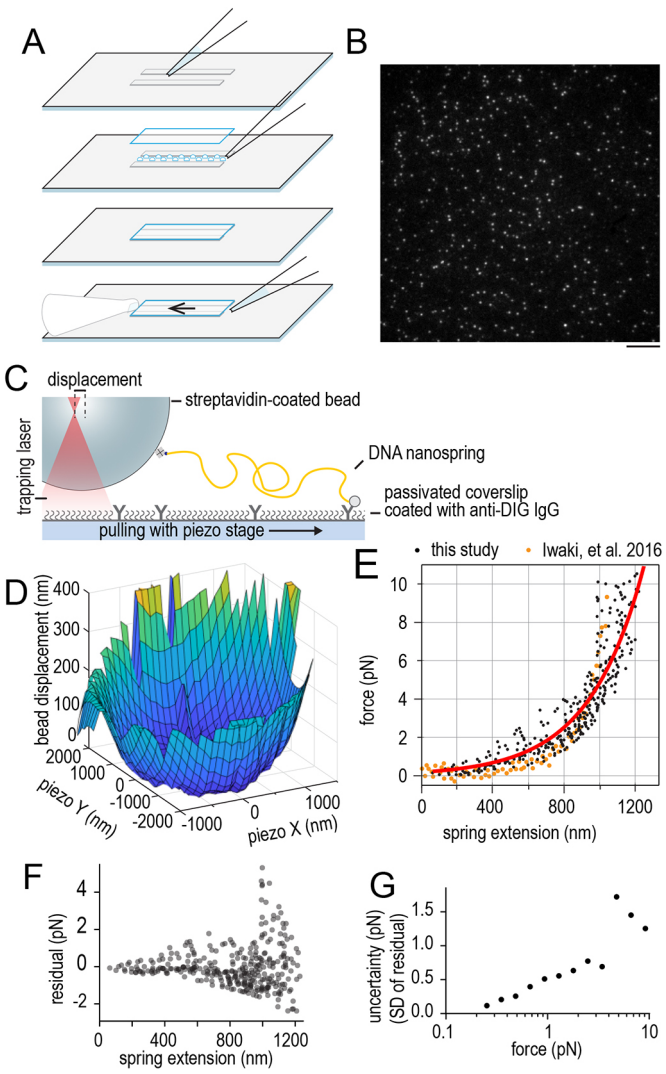

Fig. 2. Surface attachment and calibration of nanospring force–extension. (A) Schematic diagram showing assembly of a flow chamber using silanized slides and coverslips. (B) Typical microscopic field of view with 10× Atto-labelled nanosprings attached to glass surface using DIG and anti-DIG IgG. Scale bar: 10 µm. (C) Schematic diagram of an experiment with surface-bound nanospring being stretched using a bead in an optical trap. (D) A typical result (from six repeats) showing nanospring extension (vertical axis) as a function of the 2D coordinates of the microscopic stage (horizontal axes *x* and *y*). The bell-like shape of the curve signifies a single attachment point for the nanospring. (E) Force–extension curve resulting from measurements using six nanospring-attached beads (black), overlayed on top of the results presented in the original publication (orange; Iwaki et al., 2016). Solid red line shows results of exponential fitting. (F) Residuals of exponential fitting presented in E. (G) Standard deviation of residuals binned by force (as calculated from spring extension).

which we used further to convert nanospring extension into force (Fig. 2E):

$$F = 0.182\, e^{3.3x}, \quad (1)$$

where F is force in piconewtons and x is nanospring extension in micrometres. We used fitted residuals to estimate the uncertainty of force measurement from spring extension (Fig. 2F). Owing to the non-linear force–extension curve, uncertainty in force estimation increased with the nanospring extension from ±0.1 pN at forces below 0.3 pN to about ±1 pN for maximal nanospring extensions corresponding to forces above 5 pN (Fig. 2G).

Validation of nanospring-based force measurements

To benchmark the performance of the nanospring in measuring single-molecule forces, we used biotinylated dynein motor domains from *S. cerevisiae* (Reck-Peterson et al., 2006; Baclayon et al., 2017). In this experiment, the nanospring was attached to anti-DIG IgG on the coverslip via DIG, and a streptavidin-coated Qdot bound both biotinylated dynein and a biotinylated DNA staple at the end of the nanospring (Fig. 3A). We used total internal reflection fluorescence (TIRF) microscopy to record images of microtubules, Atto488-labelled nanosprings and Qdot565-bound dynein at the end of the nanospring. Owing to dimensions of the nanospring spanning several hundreds of nanometres, the best contrast was achieved using an imaging mode with deeper penetration than TIRF, such as HiLo (Tokunaga et al., 2008), or intermediate settings between TIRF and epifluorescence. Using these settings, we could readily observe spring-bound Qdots walking along the microtubule, extending the springs, and stalling upon reaching the stall force of dynein (Fig. 3B). To determine spring extensions from kymographs such as the one presented in Fig. 3B, we used two methods. First, to determine the length of the spring, in each line of a kymograph containing the Atto488 signal, we measured the centre position of pixels that were brighter than the background fluorescence level. Second, to determine the position of the end of the spring, we fitted a gaussian to each of the lines of a kymograph containing the Qdot-565 signal. Both of these measurements yielded estimates of spring extension (Fig. 3C). However, subpixel localization of the Qdot position provided less noisy data (Fig. 3D, compare magenta and yellow traces) and was therefore used in further analysis to determine the position of the spring end. Nanospring length was then converted into stalling force using Eqn 1.

As a control, we used optical trapping to measure the stall forces of bead-bound dynein (Fig. 3E). Optical trapping provided high temporal and spatial resolution (Fig. 3F); however, the stall force values extracted from both force measurement methods were similar (Fig. 3G). These results are consistent with other reports of *S. cerevisiae* dynein stall force (Gennerich et al., 2007; Laan et al., 2012).

Estimation of forces generated by growing microtubules

Growing microtubule ends recruit end-binding (EB) proteins in the shape of a comet; these comets in turn recruit a number of secondary proteins that carry EB-binding SxIP motifs (Honnappa et al., 2009). The affinity of an EB comet to SxIP-containing proteins was reported to generate sub-piconewton forces that could extend membranes, transport actin filaments along with microtubule growth and reverse the direction of a kinesin-14 motor (Rodríguez-García et al., 2020; Alkemade et al., 2022; Molodtsov et al., 2016). Although prior measurements have been performed using optical trapping, measuring sub-piconewton forces using this method is challenging, because it is easy to lose a bead from a soft trap. We therefore thought that the DNA nanospring, with its high precision in a low-force regime could provide an advantage (Fig. 2G). To couple nanospring extension to microtubule growth, we used a nanospring-bound Qdot705 coated with an mCherry-tagged and biotinylated C-terminal fragment of human MACF2 (also known as DST, hereafter just referred to as MACF) (Rodríguez-García et al., 2020) in the presence of dynamic microtubules and mCherry–EB3 (Fig. 4A). In these conditions,

Journal of Cell Science (2023) 136, jcs260154. doi:10.1242/jcs.260154

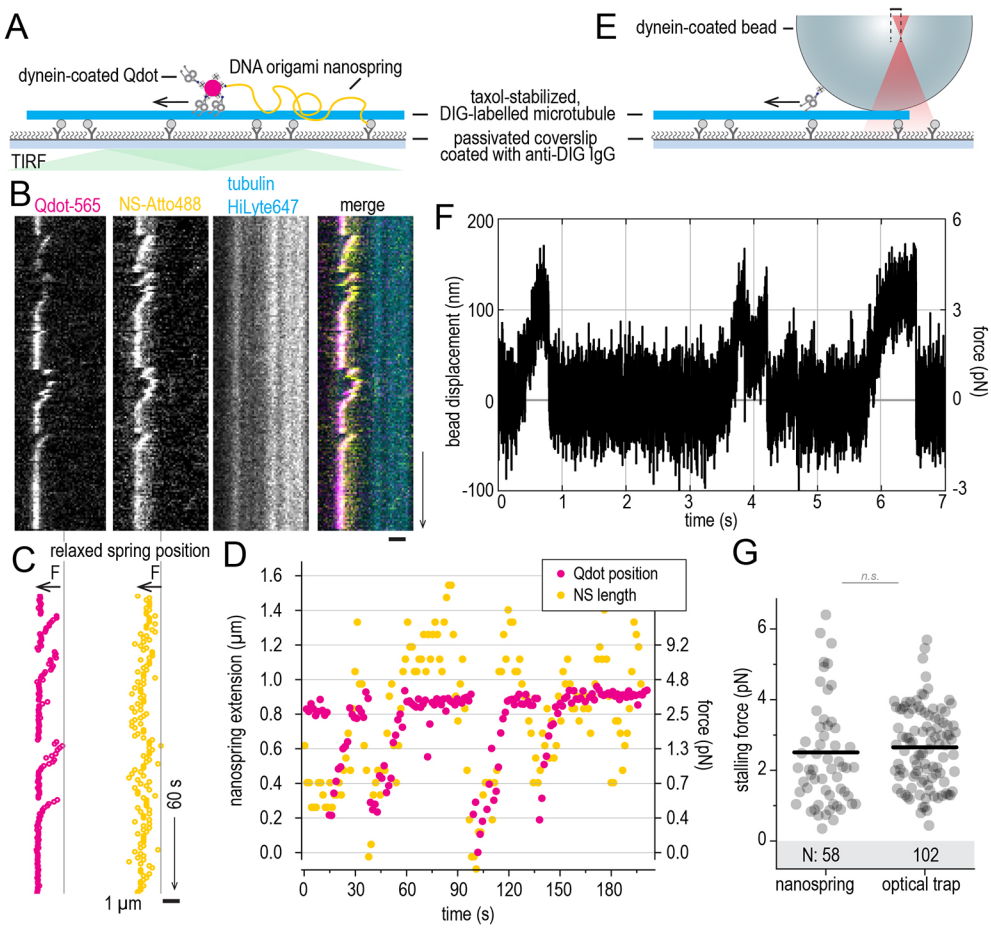

Fig. 3. Analysis of spring extension and validation of force measurements. Experiment schematics (A) and a typical kymograph from three repeats (58 force traces in total) (B) showing a coverslip-bound taxol-stabilized microtubule (cyan), Atto488-labelled nanospring (yellow) and dynein-conjugated Qdot-565 (magenta). Note that the spring spends most of the observation time in the stretched state. As the spring design we used featured 5× Atto488 at the biotinylated spring end, and 10× Atto488 along the spring length (see Fig. 1A), the fully stretched spring has one end brightly labelled, as can be seen in the Atto488 channel of the kymograph. (C) Coordinates on the nanospring end (Qdot, left), and nanospring middle (right) obtained by analysing the kymographs in B using the Julia script (see Materials and Methods for details). Vertical line shows the coordinates of the relaxed spring, arrows labelled F show direction of dynein-generated force. (D) Nanospring extension (left *y*-axis) and force (right *y*-axis) measured using these two methods and plotted as a function of time. (E) Experimental setup to estimate dynein stall force using an optical trap. (F) Typical time trace from three repeats (102 force traces in total) of a dynein walking against the applied force, recorded in an optical trap. (G) Dynein stalling forces measured using nanospring (left) and optical trapping (right). Circles, individual stall events; line: median, number of measurements is shown in the shaded area. *P*-value (two-tailed Mann–Whitney test): 0.06 (n.s., not significant). Scale bars: horizontal (1 µm), vertical (60 s) (B,C).

we observed nanosprings getting extended in the direction of microtubule growth when interacting with the mCherry–EB3 comets through mCherry–MACF (Fig. 4B). Quantification of nanospring extension using our Julia scripts, and subsequent conversion of spring extension into force yielded sub-piconewton force generation events that lasted for multiple seconds (Fig. 4C).

This experiment highlights how protein complexes at the interface of the nanospring and the microtubule end can be directly visualized using fluorescence microscopy. Our results are consistent with observations using optical trapping, where a MACF-coated bead was interacting with a growing microtubule end (Fig. 4D). In both conditions, we observed forces in sub-piconewton range lasting for many seconds (Fig. 4C,D). On average, nanospring-measured forces were smaller than optical trap-measured ones (Fig. 4F). This difference could be related to different amount of MACF molecules interacting with a comet in each case – no more than 20 in case of Qdot-nanospring, and several thousand in case of MACF-coated beads (Rodríguez-García et al., 2020).

Estimation of forces generated by microtubule shortening

We have previously shown that multimerization of the human kinetochore complex Ndc80 enables it to follow microtubule shortening against an applied force (Volkov et al., 2018). Multiple copies of Ndc80 oligomers can stall microtubule shortening, and the duration of these stalls is increased in the presence of another multi-protein kinetochore complex known as the Ska complex, which cross-links Ndc80 and microtubules (Huis in ‘t Veld et al., 2019). However, these observations were performed using bead-bound Ndc80 in an optical trap, in conditions preventing us from having precise information about the number of Ndc80 and Ska copies interacting with the force-generating microtubule ends.

To study the Ndc80–Ska–microtubule force-coupling system in single-molecule conditions, we used streptavidin-oligomerized Ndc80 bound to biotinylated nanosprings in the presence of dynamic microtubules and Ska (Fig. 5A). Using TIRF microscopy, we could simultaneously record microtubule dynamics, position of the spring-bound Ndc80, and dynamics of Ska binding to both

Journal of Cell Science (2023) 136, jcs260154. doi:10.1242/jcs.260154

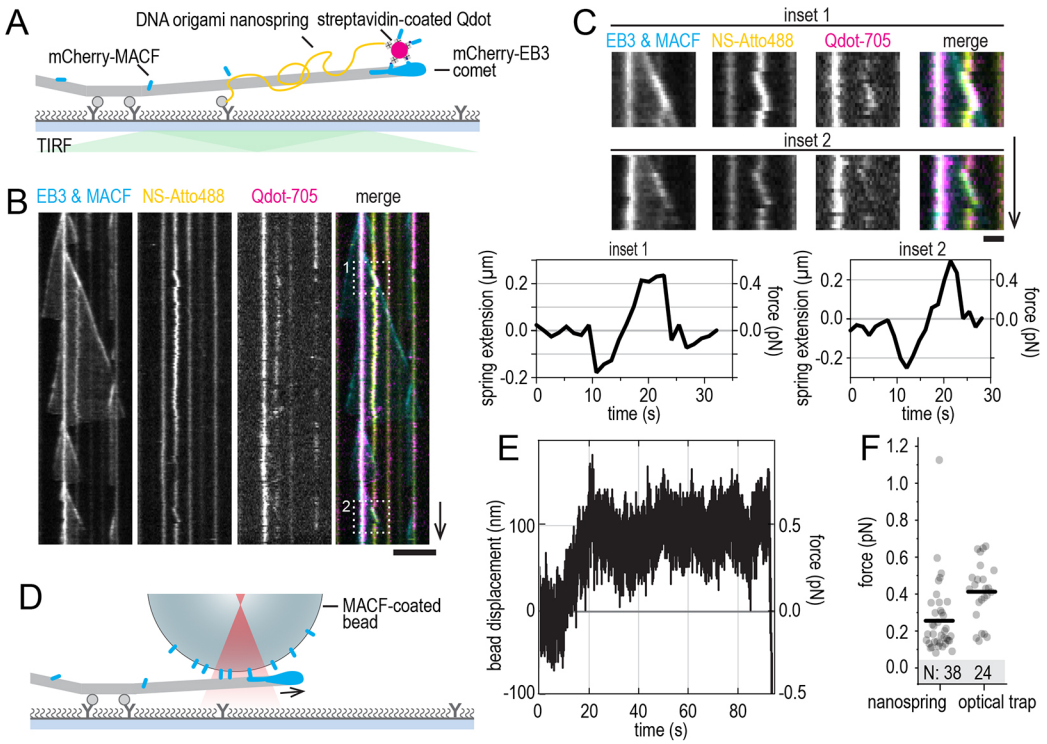

Fig. 4. Estimation of microtubule growth force using the DNA origami nanospring. Experimental setup (A) and typical kymographs from four repeats (38 force signals in total) (B); microtubules are grown from coverslip-attached GMPCPP-stabilized seeds (grey). Yellow shows the nanospring. Streptavidin-coated Qdot-705 (magenta) binds to the nanospring and is further saturated using mCherry-tagged MACF C-terminus (cyan). MACF is concentrated at the growing microtubule end thanks to the presence of mCherry-EB3 comets (cyan). Given that tubulin is unlabelled in this experiment, microtubule dynamics can be observed in MACF and EB3 channel. Boxes show events of a nanospring being stretched by growing microtubule ends. (C) Events of growing microtubule ends pulling on the nanosprings via MACF magnified from boxed regions in B. Graphs show quantification of nanospring extension and force over time for these events. (D) Experimental setup to estimate the MACF-transmitted force using the optical trap. (E) Typical time trace from three repeats (24 force signals in total) of a glass bead following microtubule growth against the applied force. (F) Forces measured in the direction of microtubule growth using MACF-conjugated nanosprings or MACF-coated beads in an optical trap. Horizontal lines show median. Scale bars: horizontal 5 µm (B) or 1 µm (C), vertical (60 s).

microtubules and Ndc80 (Fig. 5B). Note that the run length of the nanospring-bound Ndc80 was limited by the extension of the nanospring (±1 µm), restricting the previously observed distances that an Ndc80 trimer can cover with the shortening microtubule end (Volkov et al., 2018).

Forces measured using a nanospring carrying a single Ndc80 trimer in the absence of Ska were similar to previously reported forces measured using beads sparsely coated with the Ndc80 trimers in an optical trap (Fig. 5C) (Volkov et al., 2018). We then compared these forces to nanospring-measured forces recorded when Ska signals colocalized with the spring-bound Ndc80 (Fig. 5B, top), and to forces recorded in the same sample, but without Ska colocalization (Fig. 5B, bottom). As reported previously, at low Ska concentrations, the Cdk1 phosphorylation of the SKA3 C-terminus enhanced Ska–Ndc80 interactions (Huis in ‘t Veld et al., 2019), which is evident from the higher frequency of Ska-positive force events (Fig. 5C). At 100 nM Ska, Cdk1 phosphorylation was no longer necessary for Ska–Ndc80 binding; however, we did not observe a difference in nanospring-measured force resulting from the presence or absence of Ska during force development (Fig. 5C).

Presence of multiple microtubule binders at the nanospring enhances force coupling

The failure of Ska to increase the Ndc80-transmitted force was consistent with our earlier estimates using optical trapping, where the presence of Ska mainly affected the duration of stalls, and to a lesser extent the stalling force (Huis in ‘t Veld et al., 2019). We wondered, however, whether there were conditions in which we could capture higher microtubule-generated forces using nanospring-bound Ndc80. One way to increase the amount of transmitted force is to engage more copies of a force-coupling molecule (Volkov et al., 2018; Volkov, 2020). To test this hypothesis, we sought to increase the multimerization of Ndc80 at the end of the spring.

We took advantage of the SpyCatcher–SpyTag interactions forming a covalent bond, and a previously described protocol to biochemically separate streptavidin tetramers refolded from mixtures of SpyCatcher–avidin, SpyTag–avidin and Traptavidin (Chivers et al., 2010; Fairhead et al., 2014). We first expressed, refolded and purified streptavidin tetramers containing three SpyTag–avidin subunits and one Traptavidin subunit (T_1S_{T3}) and then mixed these with an excess of SpyCatcher avidin tetramers (S4) (Fig. 6A; Fig. S1A,B). The resulting $T_1S_{T3}S_{12}$ scaffolds were mixed with an excess of $Ndc80^{SpyTag}$ to generate objects containing up to nine Ndc80 copies. Ndc80 was labelled with TMR using sortase and a fluorescently labelled peptide in the same reaction and the final product, $T_1S_{T3}S_{12}[Ndc80]_x$, was purified using a glycerol gradient (Fig. 6A; Fig. S1B,C). Examining the resulting Ndc80 multimers by electron microscopy, we found Ndc80 multimers with varying stoichiometries. Typical Ndc80 multimers contained four to seven Ndc80 arms (Fig. 6C).

Attaching these multivalent objects to the biotinylated nanosprings, we could measure the force they transmitted from the microtubule shortening, and their brightness (Fig. 6D).

Journal of Cell Science (2023) 136, jcs260154. doi:10.1242/jcs.260154

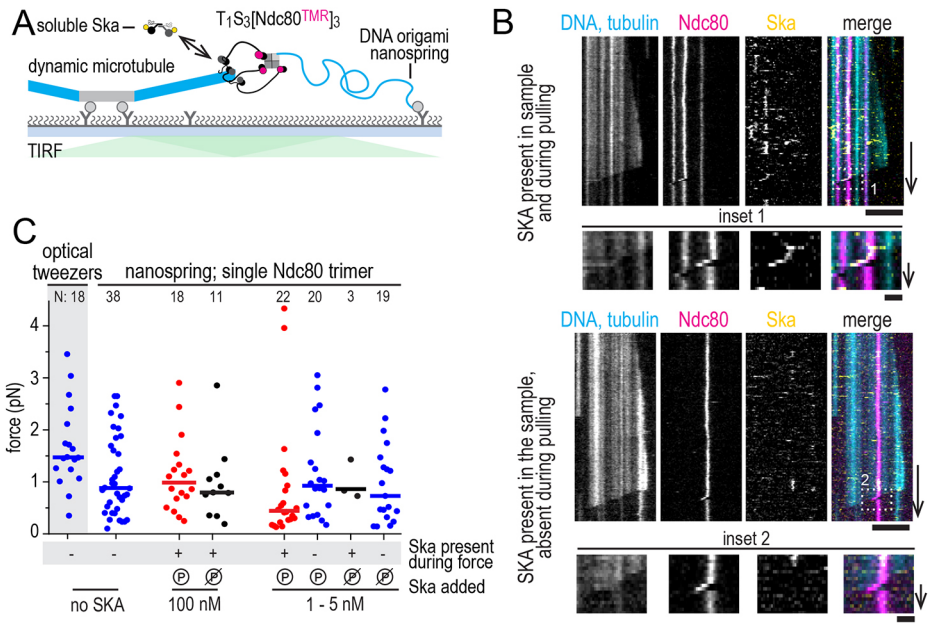

Fig. 5. Estimation of microtubule shortening force using DNA origami nanospring. (A) Experimental setup. GMPCPP-stabilized microtubule seeds (grey) are attached to the coverslip and nucleate dynamic fluorescently labelled microtubules (cyan). An Atto488-labelled nanospring (cyan) is conjugated to Ndc80–TMR trimers (magenta) oligomerized using streptavidin. Ska complex labelled with HiLyte-647 (yellow) is present in solution and can bind both to Ndc80 and to microtubules. (B) Typical results from five repeats showing shortening microtubule ends pulling on nanospring-conjugated Ndc80 trimers (boxes). Top example, Ska is bound to the Ndc80 trimer during force development. Bottom example, Ska is present in the sample, but not bound to the Ndc80 trimer during force development. Boxed regions are magnified below the full kymographs. (C) Forces measured using a single Ndc80 trimer following microtubule shortening against the force exerted by the stretched nanospring. Shaded area, stalling forces measured using beads sparsely coated with Ndc80 trimers in an optical trap (Volkov et al., 2018). Circles, individual measurements; lines, median. Cdk1 phosphorylation of SKA3 leads to increased recruitment of Ska to Ndc80 trimers during force development (Huis in 't Veld et al., 2019), but has no effect on the measured force within the Ska concentrations in the range between 1 and 100 nM. Scale bars: horizontal 5 µm (B), 1 µm (insets), vertical 60 s (B), 10 s (magnified views).

Consistent with our observations by EM, the distribution of Ndc80 copy number was quite wide, peaking at six Ndc80 copies per object (Fig. 6E). Consistent with increased Ndc80 copy numbers, Ndc80 multimers transmitted up to 10 pN of microtubule-generated force, compared to a maximum of 3 pN transmitted by a single Ndc80 trimer (Fig. 6F). Contrary to the experiments with bead-bound Ndc80 trimers, we did not observe force-dependent microtubule rescue with Ndc80 multimers bound to nanosprings despite forces in the 5–10 pN range.

DISCUSSION

Classically, force production by the mitotic spindle and force sensitivity of the mitotic checkpoint were studied using microneedles inserted into a dividing cell (Li and Nicklas, 1995; Nicklas, 1983). Recent developments of this approach yielded important insights into the organization of mitotic spindle (Long et al., 2020; Suresh et al., 2020), but precise quantification of forces *in vivo* remains challenging. Alternatively, tension at the centromeric region of the chromosomes can be estimated indirectly, based on assumptions about stiffness of stretchable elements in the cells (Harasymiw et al., 2019; Mukherjee et al., 2019).

The third method of estimating microtubule-generated tension *in vivo* is based on Förster resonance energy transfer (FRET) sensors. With a FRET sensor, the efficiency of energy transfer between donor and acceptor fluorophores depends on the distance between these fluorophores, allowing reading out tension using fluorescence intensity of the acceptor fluorophore (Cost et al., 2015; Grashoff et al., 2010). Although the FRET approach provides important evidence regarding the role of tension in regulating the kinetochore–microtubule attachments *in vivo*, multiple copies of microtubule binders interacting with multiple microtubule ends result in ensemble readouts that are challenging to interpret at the single-molecule level (Kuhn and Dumont, 2019; Liu et al., 2009; Suzuki et al., 2016; Ye et al., 2016; Yoo et al., 2018).

The DNA nanospring is a force sensor that outputs a force signal directly through measurement of its extension. Potential advantages of nanosprings include multiplexed force measurements in a single microscopic field of view, simultaneous visualization of additional factors being recruited during force production (Fig. 5), and implementation in laboratories without access to an optical trap. Compared to an optical trap, nanosprings have a lower time resolution, limited to 1–100 Hz by the frame rate of the timelapse image acquisition as opposed to the kilohertz range in an optical trap. At the same time, the use of the nanospring alleviates concerns related to the 'lever arm' effects arising from the geometry of microtubule–bead connection (Volkov et al., 2013; Pyrpassopoulos et al., 2020).

Because of a non-linear force–extension curve (Iwaki et al., 2016), the nanospring provides a particularly clear readout in the sub-piconewton force range. This enabled us to measure forces generated by a protein complex tracking growing microtubule ends (Fig. 4). Although the same phenomenon could also be observed using optical trapping (Alkemade et al., 2022; Molodtsov et al., 2016; Rodríguez-García et al., 2020), measurement of such small forces is usually technically challenging. It should be noted that at higher extensions (and higher forces), nanosprings are less precise than optical tweezers in force estimation (uncertainty up to ±1 pN at above 5 pN, Fig. 2G, compared to ∼0.1 pN or lower for optical tweezers).

Journal of Cell Science (2023) 136, jcs260154. doi:10.1242/jcs.260154

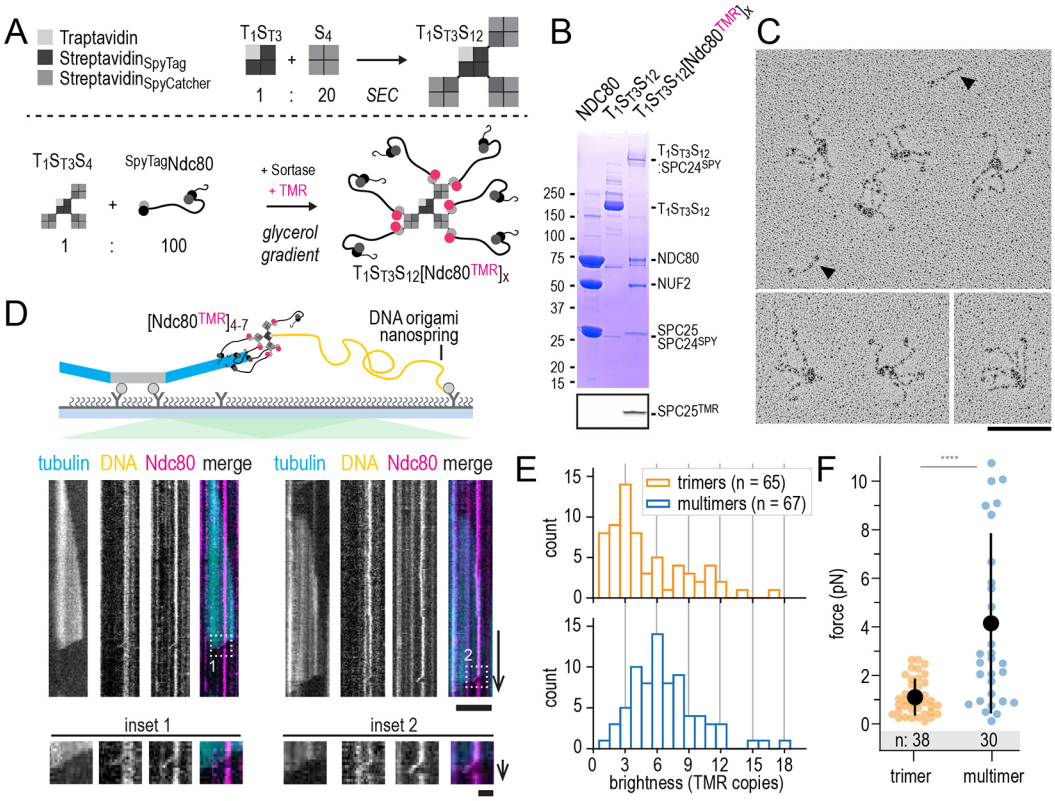

Fig. 6. Presence of multiple microtubule-binders at the nanospring enhances force-coupling. (A) $T1S_T3S_C12$ assemblies were generated from $T1S_T3$ and S_C12 tetramers, purified using size-exclusion chromatography, and incubated with Ndc80. See Fig. S1 for more information. (B) The final product, $T1S_T3S_C12[Ndc80^{TMR}]_x$ containing up to nine Ndc80 copies, is also shown side-by-side with monomeric Ndc80 and the spy-avidin scaffold. The top gel image is taken after Coomassie staining and the bottom is the image of the same gel taken at 561 nm fluorescence channel. Streptavidin remains tetrameric during SDS-PAGE given that samples were not heated before analysis. The four subunits of the Ndc80 complex (NDC80, NUF2, SPC24 and SPC25), however, run separately, as their interactions are broken in the presence of SDS. (C) Multimeric Ndc80 assemblies were purified on a density gradient and inspected by electron microscopy after low-angle platinum shadowing. Monomeric Ndc80 complexes (arrowheads) are shown next to multimeric Ndc80 modules. The sample shown in B and C was used for experiments presented in D–F. (D) Experimental setup and typical kymographs from five repeats showing DNA nanosprings (yellow) extended by Ndc80 multimers (magenta) following the shortening ends of dynamic microtubules (cyan). Enlarged images of the indicated regions shown are magnified below the full kymographs. (E) Brightness of Ndc80 trimers (orange) and multimers (blue) expressed as a copy number of Ndc80-TMR. (F) Forces calculated from nanospring extension for a single Ndc80 trimer (orange) and a single Ndc80 multimer (blue). Black circles show mean, error bars show s.d. *P*-value (two-tailed Mann–Whitney test): 2.2×10^{-5} (****, $<10^{-4}$). Scale bars: horizontal 100 nm (C), 5 µm (D), 1 µm (magnified views in D), vertical 60 s (D), 10 s (insets in D).

Forces generated by shortening microtubules can sometimes exceed 10 pN (Akiyoshi et al., 2010; Volkov et al., 2013), the upper limit of the force–extension curve for the nanospring (Fig. 2E). At higher forces, the DNA origami structure might unfold (Engel et al., 2018) or detach from its surface anchor (Neuert et al., 2006). A possible improvement of the attachment strength could be obtained by using DIG10.3 instead of anti-DIG IgG (Tinberg et al., 2013; Van Patten et al., 2018). In addition, multiple DIG- and biotin-labelled staples could be introduced to share the load evenly. In our experience, the DNA origami nanosprings were stable in microtubule force experiments for up to 30–60 min. To further improve the lifetime of the nanospring under force, ligation (Ramakrishnan et al., 2019) or chemical crosslinking of strands (Rajendran et al., 2011; Thomas et al., 2022) after purification could be beneficial.

In this study, nanosprings provided similar force amplitude values to those in published optical trapping experiments in different experimental settings. MACF-mediated force transmission resulted in consistently lower forces produced by microtubule growth and measured using the nanospring. We hypothesise that the nanospring could be particularly sensitive in the sub-piconewton regime, where extension of the spring within the 200–300 nm range leads to estimation of the force with ∼0.1 pN accuracy (Fig. 2F,G).

Ndc80 oligomers attached to nanosprings did not rescue microtubule depolymerization under force (Figs 5, 6), in contrast to our previous experiments where beads densely coated with Ndc80 rescued microtubule shortening under force (Volkov et al., 2018). In experiments with beads, the exact copy number of microtubule-coupled Ndc80 is unknown. The direct quantification of Ndc80 copy number at the interface between the nanospring and the dynamic microtubule end allows us to conclude that the presence of additional copies of Ndc80, but not Ska, correlates with an increase in the force transmitted by a shortening microtubule. Increased force captured by the nanospring, however, did not result in an increased rescue frequency, consistent with our systematic analysis of microtubule rescue mechanisms, which revealed the stall duration, rather than stall force, was the most reliable predictor of rescue (Huis in ‘t Veld et al., 2019). It is possible that the DNA springs were too unstable at high forces to sustain a stall long enough to produce a microtubule rescue, or that more than nine copies of Ndc80 are necessary to reliably prevent re-initiation of shortening after a short stall. Mechanistic insight into these questions requires further experiments.

Journal of Cell Science (2023) 136, jcs260154. doi:10.1242/jcs.260154

In summary, we demonstrate the use of the DNA origami nanospring in measuring the force of microtubule motors walking along a stable microtubule lattice, as well as the forces exerted by dynamic microtubule ends via proteins following their growth or shortening. In addition, we extend the use of this method to recording single-molecule dynamics of proteins binding and unbinding at the site of force generation. We conclude that the DNA origami nanospring is a powerful tool to study transmission and sensing of microtubule-generated forces *in vitro*.

MATERIALS AND METHODS

Design and purification of the DNA nanospring

The originally described DNA nanospring design is based on the M13mp18 single-stranded DNA scaffold (Iwaki et al., 2016), but it could also be adapted to other commercially available scaffolds such as p7560 using caDNAno software (Douglas et al., 2009) and the json file describing the original design.

Step-by-step protocol for modification of the spring design using a different single-stranded DNA scaffold, or to re-staple using a different set of DNA oligonucleotides is:

- Open the .json file in caDNAno; on the left, in the slice panel, you will see six cells are highlighted. This is the cross-section view of potential helices. The right panel (path panel) shows the side view of the DNA construct with cells representing DNA bases. In this design, there are only two DNA double strands being formed, 0 and 1 (Fig. 1A).
- Zoom in the cells 0 and 1 in the path panel to see DNA strands. The blue line shows the single-strand DNA scaffold that will be folded on itself over cells 0 and 1 via staple DNA oligonucleotides, which are shown in dark grey.
- Go to the right terminal of scaffold (hold control/command and drag) where you can see the 3′ end (represented as an arrow in caDNAno) and the 5′ end (a square).
- Choose the ‘select’ tool in the control bar in the right and click on the 3′ arrow. Once it is selected, the arrow turns red. Now you can drag the arrow to extend the scaffold (Fig. 1Bi). If there is not enough space to extend the strand, go to the rightmost part of the grid and click on the double head arrow. Then you can add more bases to the grid (should be a multiple of 21).
- Repeat the previous step for the 5′ square. Keep in mind that the total length of the blue line should not exceed the length of the actual single-stranded (ss)DNA scaffold.
- Tip: hold the ALT key and click on 3′ or 5′ ends to push them to the extremes of the grid.
- In this design, a hairpin of three bases is introduced at every 14 bases in one of the scaffold strands (strand 1). Extend this pattern in the newly added bases by clicking on ‘Insert’ in the left bar and then clicking on every 14 squares in the grid (Fig. 1Bi).
- Click on hairpins and type the number of bases that you want to have in the hairpin (3). Press Enter to apply. Varying the length of the hairpins will affect the twisting of the resulting spring (Fig. 1Bii).
- At this point it is possible to use the ‘Auto Staple’ tool on the top bar to generate folding staples and distribute them over the scaffold, but this also resets the present design of staples. Alternatively, you can add staples manually using the ‘Pencil’ tool. Following the existing pattern, insert a complementary oligonucleotide next to strands 0 and 1. Connect the oligos by dragging the 3′ of one of them and releasing it over 5′ of the opposite oligonucleotide on the other strand of scaffold. This creates a circular oligonucleotide that connects two scaffold strands (Fig. 1Biii).
- Since linear oligonucleotides will be used to fold the scaffold, they need to be broken at a certain site. In the current design the breaking site is 11 bases away from the nearest left crossover. Select the ‘Break’ tool and click on this site to generate the break (Fig. 1Biv). The ‘Auto break’ tool can be used for the same purpose, but the break sites will be decided by the program and propagated to the whole design, overriding manual settings.
- If you want to use the same staples as for the shorter nanospring, you should count how many bases have been added to the 5′ path of scaffold in caDNAno design. Cut the same number of the bases from the 3′ end of the scaffold sequence and paste it before the 5′ terminal of the sequence.

Depending on the scaffold used (i.e. M13mp18, p7308, p7560, p7704, p8064, p8100 or p8634) and on the starting position in the scaffold, the same design produces different staple sequences. We provide a json file describing the nanospring design at https://github.com/volkovdelft/kymo.jl.

The scaffold and staple DNA oligonucleotides were obtained from Tilibit Nanosystems. The nanospring was folded by mixing 20 nM scaffold and 200 nM staples in the folding buffer (40 mM Tris-HCl pH 8.0 with 1 mM EDTA and 12 mM $MgCl_2$) followed by an incubation in a thermocycler (80°C for 10 min, gradient from 80°C to 60°C over 2 h, gradient from 60°C to 20°C over 2 h). Folded DNA nanosprings were separated from excess staples and partially folded products on a 1% agarose gel in Tris-Borate-EDTA buffer supplemented with 12 mM $MgCl_2$. Nanospring-containing bands were excised and extracted from the gel using Freeze ‘N Squeeze™ DNA gel extraction spin columns (Bio-Rad).

Negative stain electron microscopy

A solution of purified nanosprings (3 µl) was placed on a recently glow-discharged grid with a continuous layer of carbon, blotted and immediately washed three times, followed by the application of 3 µl of the 2% uranyl acetate solution for 3 min. The grids were then blotted once more with a blotting paper and dried for 20 min. Images were acquired on a JEOL JEM1200 microscope equipped with a TVIPS *F*416 camera at a nominal magnification of 41,000×, resulting in a pixel size of 0.38 nm.

Protein expression and purification

The dynein motor domain was purified and biotinylated as described previously (Baclayon et al., 2017; Reck-Peterson et al., 2006). EB3 and the MACF2 C-terminus was expressed and purified as described previously (Rodríguez-García et al., 2020). Ndc80 and Ska were expressed and purified, and Ndc80 was assembled into trimers as described previously (Huis in ‘t Veld et al., 2019; Volkov et al., 2018).

Assembly of multimeric Ndc80 modules

Subunits of spyavidin scaffolds were expressed using Traptavidin, Dead-Streptavidin-SpyCatcher, Dead-Streptavidin-SpyTag and Traptavidin-E6 plasmids. These plasmids were generated by the Howarth laboratory (Chivers et al., 2010; Fairhead et al., 2014), we obtained them through Addgene (26054, 59547, 59548 and 59549).

$T1S_C3$, $T1S_T3$ tetramers and S_C4 modules were prepared as described previously (Fairhead et al., 2014). To generate multimeric $T1S_T3S_C12$ Spyavidin scaffolds, $T1S_T3$ and S_C4 tetramers were mixed and purified by size-exclusion chromatography (Superose 6 10/300) as detailed in Fig. S1A,B.

Ndc80 with $SPC24^{SpyTag}$ and $SPC25^{SortaseHis}$ was incubated at 30 µM with $T1S_T3S_C12$ assemblies at 0.3 µM in a 16 h reaction at 10°C in Ndc80 buffer containing 20 mM Tris-HCl pH 8, 200 mM NaCl, 2% glycerol (v/v) and 2 mM TCEP. Protease inhibitor (HP PLUS, Serva 39107) was present at 2.5-fold the recommended concentration. 5 M Sortase (Hirakawa et al., 2015), Ca^{2+} and GGGGK-TMR peptide (Genscript) were added at concentrations of 10 µM, 10 mM and 150 µM, respectively, to fluorescently label Ndc80. The reaction volume was 1 ml and reaction progress was monitored as detailed in Fig. S1C.

$T1S_T3S_C12(Ndc80)_x$ modules were separated from monomeric Ndc80 on a 15–50% glycerol gradient of ∼12 ml in a SW40 rotor (Beckman) at 40,000 rpm for 16 h at 4°C. Manually collected fractions were analysed as detailed in Fig. S1C and selected fractions were pooled, frozen in liquid nitrogen, and stored at −80°C until further use. Shadowing electron microscopy was performed as described previously (Huis in ‘t Veld et al., 2016).

Coverslip and slide passivation

Glass slides and coverslips were treated with oxygen plasma for 3 min in a PSI Plasma Prep III plasma cleaner at 60 mTorr, 20–50W. Immediately after plasma treatment, the coverslips were immersed into a repel-silane solution

Journal of Cell Science (2023) 136, jcs260154. doi:10.1242/jcs.260154

(2% dichlorodiethylsilane in trichloroethylene or octamethylcyclooctasilane) for 5 min (Gell et al., 2010; Volkov et al., 2014). After the incubation, silanized coverslips were transferred to 96% ethanol solution and sonicated in a water bath sonicator for 20 min, following by 5–10 rinses with purified water. Silanization was considered successful if the glass was almost dry when emerging from water. Slides and coverslips were dried and stored for up to 2 months.

Assembly of flow chambers and attachment of nanosprings to the coverslip surface

Silanizing both slides and coverslips provides superior control of non-specific adsorption of proteins to glass but presents a challenge when introducing water solutions into a pre-assembled hydrophobic flow chamber. To overcome this, we used the following sequence. Anti-DIG IgG (Roche 11333089001) diluted in in MRB80 (80 mM K-PIPES pH 6.9, 1 mM EGTA, 4 mM $MgCl_2$) to a final concentration of 0.2 µM was placed in 0.5–1 µl drops between the strips of double-sided tape (10–15 µl in total) and covered with a piece of silanized coverslip, followed by a 15 min incubation. The chamber was washed with 100 µl MRB80, then with 50 µl 1% Pluronic F-127 in MRB80 and incubated further for 20–60 min (Fig. 2A). Finally, 10 µl of nanospring diluted in MRB80 was added. Fig. 2B shows a microscopic field of view after addition of Atto-488 labelled nanosprings diluted 1:10 from a 5 nM stock solution. Alternatively, surface passivation after silanization can be achieved by replacing 1% Pluronic F-127 with 1% Tween-20. Tween-20 passivation was shown to be particularly effective against non-specific adsorption of streptavidin (Hua et al., 2014).

Experiments with dynein

Taxol-stabilized microtubules were prepared by polymerization of 50 µM tubulin (with 5–10% fluorescent- and DIG-labelled tubulin) in MRB80 supplemented with 1 mM GTP and 25% glycerol for 20 min at 37°C, followed by addition of 25 µM taxol and another 10–20 min incubation. Microtubules were sedimented in a Beckman Airfuge at 14 psi for 3 min and resuspended in MRB80 with 40 µM taxol.

To conjugate nanospring with Qdot and dynein, 4.5 µl nanospring was mixed with 0.5 µl streptavidin-Qdot (final concentration 100 nM) on ice for several hours or overnight. Biotinylated dynein (final concentration 1–20 nM) was mixed with 50 µl MRB80 with 1 mM ATP, 1 mM DTT and 0.5 mg/ml κ-casein (Sigma-Aldrich), spun in a Beckman Airfuge (30 psi, 5 min), and 5 µl of the supernatant was mixed with 5 µl Qdot-nanospring reaction from the previous step.

A flow-chamber prepared with silanized slides and coverslips and passivated with 1% Tween-20 as described above was filled with nanospring-Qdot-dynein reaction supplemented with 0.5 mg/ml κ-casein. After washing with MRB80 with 0.5 mg/ml κ-casein, taxol-stabilized microtubules were added and incubated for 3 min, followed by another wash with MRB80 with 0.5 mg/ml κ-casein. Finally, the chamber was filled with imaging buffer (MRB80 with 1 mg/ml κ-casein, 50 mM KCl, 1 mM ATP, 40 µM taxol, 20 mM glucose, 4 mM DTT, 0.2 mg/ml catalase, 0.4 mg/ml glucose oxidase).

Experiments with MACF2

GMPCPP seeds were polymerized by incubating 25 µM tubulin (40% DIG-labelled, total volume 8 µl) and 1 mM GMPCPP (Jena Biosciences) for 30 min at 37°C. Polymerized microtubules were sedimented in a Beckman Airfuge (30 psi, 5 min), and the pellet was resuspended on ice in 6 µl MRB80 with addition of 1 mM GMPCPP, followed by a 30 min incubation on ice. The reaction was then transferred to 37°C, and microtubules polymerized for 30 min and sedimented as above. The pellet was resuspended in 50 µl MRB80 with 10% glycerol, and aliquots snap-frozen in liquid nitrogen and stored at −80°C for up to 3 months.

Nanosprings were first attached to Qdots as described above. After an incubation on ice, biotinylated MACF2 C-terminus was added at 1 µM to saturate remaining biotin-binding sites on the Qdots. Flow chambers were assembled from silanized slides and coverslips and passivated with 1% Tween-20 as described above. The nanospring-Qdot-MACF reaction was then supplemented with 0.5 mg/ml κ-casein and added to the chamber, the chamber was transferred to 37°C. Tubulin polymerization mix containing 15 µM tubulin, 1 mg/ml κ-casein, 0.01% methylcellulose, 1 mM GTP, 20 mM glucose, 4 mM DTT, 0.2 mg/ml catalase, 0.4 mg/ml glucose oxidase, 50 mM KCl, 100 nM EB3 and 15 nM MACF was cleared by centrifugation in a Beckman Airfuge (30 psi, 5 min). Cleared tubulin mix was added to GMPCPP-stabilized seeds and incubated for 10 min at 37°C. Finally, polymerized microtubules were added to the pre-warmed chamber, the chamber was sealed and immediately imaged.

Experiments with Ndc80 and Ska

Nanospring–Ndc80 trimer conjugation was set up by mixing 10 µl Ndc80 buffer NB (50 mM NaHepes pH 7.5 with 250 mM NaCl and 5% glycerol) with 1 µl nanospring, 0.5 mg/ml κ-casein, 1 mM DTT and 100-200 nM Ndc80 trimers, followed by an incubation for 1–3 h on ice. The flow chamber was assembled using silanized slides and coverslips, and passivated with 1% Tween-20 as described above. Tubulin polymerization mix was prepared by mixing 1 mg/ml κ-casein, 0.01% methylcellulose, 1 mM GTP, 20 mM glucose, 4 mM DTT, 0.2 mg/ml catalase, 0.4 mg/ml glucose oxidase and 8–10 µM tubulin (5–10% fluorescently labelled) and clearing it in a Beckman Airfuge (30 psi, 5 min). GMPCPP seeds were then added to this mix and incubated at 37°C to start microtubule polymerization (optionally, with addition of 1-100 nM Ska).

The passivated flow-chamber was washed with 100 µl buffer NB, then with 50 µl buffer NB with 0.5 mg/ml κ-casein and 1 mM DTT. The nanospring–Ndc80 reaction was diluted by adding 3 µl to 7 µl NB with 0.5 mg/ml κ-casein and 1 mM DTT (dilution tuned based on desired nanospring density), and added to the chamber for 3–5 min, followed by a wash with 100 µl MRB80 with 0.5 mg/ml κ-casein and 1 mM DTT. The chamber was then pre-warmed at 37°C, followed by addition of pre-polymerized microtubules and seeds, immediately sealed and imaged at the microscope.

Imaging and image analysis

Images were acquired using Nikon Ti-E microscope (Nikon, Japan) with the perfect focus system (Nikon) equipped with a Plan Apo 100×1.45 NA TIRF oil-immersion objective (Nikon), iLas2 ring TIRF module (Roper Scientific) and an Evolve 512 EMCCD camera (Roper Scientific). The sample was illuminated with 488 nm (150 mW), 561 nm (100 mW) and 642 nm (110 mW) lasers through a quad-band filter set containing a ZT405/488/561/640rpc dichroic mirror and a ZET405/488/561/640 m emission filter (Chroma). Images were acquired sequentially with MetaMorph 7.8 software (Molecular Devices, San Jose, CA). The final resolution was 0.107 µm/pixel, using an additional 1.5× lens. The objective was heated to 34°C by a custom-made collar coupled with a thermostat, resulting in the flow chamber being heated to 30°C. TIRF penetration depth was fine-tuned separately for each fluorescent channel.

Further analysis was undertaken in Fiji software (Schindelin et al., 2012) and using Julia using custom scripts available at https://github.com/volkovdelft/kymo.jl. Kymographs were made through a reslice operation using the kymograph_3channel.ijm macro. Position of the nanospring end was determined by running kymoNS.ipynb in a jupyter notebook and following in-line comments. In brief, the script opens the kymograph and waits for the user to (1) select a portion of the kymograph with only one particle to trace, and (2) select a 'background' region and the initial position of the particle. Then each line of the kymograph is fitted to a gaussian to determine localization of a particle and its brightness.

Preparation of beads and optical trapping

Glass 1 µm beads were covalently bound to poly-L-lysine grafted with biotinylated poly-ethyleneglycole (PLL-PEG) as described previously (Volkov et al., 2018). Biotin molecules on the bead surface were then saturated with neutravidin. Optical trapping was performed using a custom instrument described before (Baclayon et al., 2017). To calibrate the nanospring force–extension curve, neutravidin-coated beads were introduced into a flow-chamber with a DIG–nanospring–biotin bound to the surface through anti-DIG-IgG (see above). After a bead was trapped, the piezo stage was moved manually in 100-nm steps to scan the bead

displacements around the nanospring attachment point. Successful attachment of a bead to exactly one spring produced a bell-shaped displacement profile, like the one shown in Fig. 2D. Beads producing other types of profiles (interpreted as attachment to the coverslip, or to more than one spring) were discarded from further analysis.

For experiments with dynein, biotinylated dynein motor domains were bound to streptavidin-coated PLL-PEG beads. We tuned surface density of dynein such that 30% or fewer beads interacted with a microtubule, ensuring predominantly single-motor events. Experiments were performed in a buffer that contained MRB80 with 1 mg/ml κ-casein, 50 mM KCl, 1 mM ATP, 40 µM taxol, 20 mM glucose, 4 mM DTT, 0.2 mg/ml catalase and 0.4 mg/ml glucose oxidase. The position of the bead was recorded with a quadrant photo detector at 10 kHz, and simultaneously using differential interference microscopy to monitor bead-microtubule interaction. Experiments with MACF-coated beads were performed as described previously (Rodríguez-García et al., 2020).

Acknowledgements
We are grateful to Jean-Philippe Sobczak (Tilibit Nanosystems) for discussions and assistance with design of the modified nanosprings, to Ruben Kazner and Isabelle Stender (MPI Dortmund) for assistance preparing Ndc80 multimers, and to Nemo Andrea (TU Delft) for help with negative stain EM. We also thank Marian Baclayon and Esengül Yildirim (TU Delft) for dynein purification, and Andrea Musacchio and members of the Dogterom lab for discussions.

Competing interests
The authors declare no competing or financial interests.

Author contributions
Conceptualization: V.A.V., A.N.M., P.J.H.; Methodology: V.A.V., P.J.H. ; Software: V.A.V.; Validation: A.N.M., V.A.V.; Formal analysis: V.A.V.; Investigation: A.N.M., P.J.H., V.A.V.; Resources: A.N.M., P.J.H., A.A., M.D., V.A.V.; Data curation: A.N.M., P.J.H., V.A.V.; Writing – original Draft: A.N.M., V.A.V.; Writing – editing & review: A.N.M., P.J.H., A.A., M.D., V.A.V.; Visualization: A.N.M., P.J.H., V.A.V.; Supervision: V.A.V.; Project administration: V.A.V.; Funding acquisition: A.A., M.D.

Funding
This work was supported by a European Molecular Biology Organization (EMBO) short-term fellowship (grant 7203) to P.J.H., a European Research Council Synergy Grant MODELCELL (grant 609822) to M.D. and A.A., and by a Queen Mary University of London (QMUL) startup grant SBC8VOL2 to V.A.V.

Data availability
Image analysis code is available from GitHub: https://github.com/volkovdelft/kymo.jl. Imaging data are available from Zenodo: https://doi.org/10.5281/zenodo.6977065.

Peer review history
The peer review history is available online at https://journals.biologists.com/jcs/lookup/doi/10.1242/jcs.260154.reviewer-comments.pdf.

References
Akiyoshi, B., Sarangapani, K. K., Powers, A. F., Nelson, C. R., Reichow, S. L., Arellano-Santoyo, H., Gonen, T., Ranish, J. A., Asbury, C. L. and Biggins, S. (2010). Tension directly stabilizes reconstituted kinetochore-microtubule attachments. *Nature* **468**, 576-579. doi:10.1038/nature09594

Alkemade, C., Wierenga, H., Volkov, V. A., Preciado López, M., Akhmanova, A., ten Wolde, P. R., Dogterom, M. and Koenderink, G. H. (2022). Cross-linkers at growing microtubule ends generate forces that drive actin transport. *Proc. Natl. Acad. Sci. USA* **119**, e2112799119. doi:10.1073/pnas.2112799119

Audett, M. R. and Maresca, T. J. (2020). The whole is greater than the sum of its parts: at the intersection of order, disorder, and kinetochore function. *Essays Biochem.* **64**, 349-358. doi:10.1042/EBC20190069

Baclayon, M., Kalisch, S.-M., Hendel, E., Laan, L., Husson, J., Munteanu, E. L. and Dogterom, M. (2017). Optical tweezers-based measurements of forces and dynamics at microtubule ends. In *Optical Tweezers: Methods and Protocols* (ed. A. Gennerich), pp. 411-435. New York, NY: Springer New York.

Chivers, C. E., Crozat, E., Chu, C., Moy, V. T., Sherratt, D. J. and Howarth, M. (2010). A streptavidin variant with slower biotin dissociation and increased mechanostability. *Nat. Methods* **7**, 391-393. doi:10.1038/nmeth.1450

Cost, A.-L., Ringer, P., Chrostek-Grashoff, A. and Grashoff, C. (2015). How to measure molecular forces in cells: a guide to evaluating genetically-encoded FRET-based tension sensors. *Cell. Mol. Bioeng.* **8**, 96-105. doi:10.1007/s12195-014-0368-1

Deng, Y. and Asbury, C. L. (2017). Simultaneous manipulation and super-resolution fluorescence imaging of individual kinetochores coupled to microtubule tips. In *Optical Tweezers: Methods and Protocols* (ed. A. Gennerich), pp. 437-467. New York, NY: Springer New York.

Douglas, S. M., Marblestone, A. H., Teerapittayanon, S., Vazquez, A., Church, G. M. and Shih, W. M. (2009). Rapid prototyping of 3D DNA-origami shapes with caDNAno. *Nucleic Acids Res.* **37**, 5001-5006. doi:10.1093/nar/gkp436

Engel, M. C., Smith, D. M., Jobst, M. A., Sajfutdinow, M., Liedl, T., Romano, F., Rovigatti, L., Louis, A. A. and Doye, J. P. K. (2018). Force-Induced Unravelling of DNA Origami. *ACS Nano* **12**, 6734-6747. doi:10.1021/acsnano.8b01844

Fairhead, M., Veggiani, G., Lever, M., Yan, J., Mesner, D., Robinson, C. V., Dushek, O., van der Merwe, P. A. and Howarth, M. (2014). SpyAvidin Hubs Enable Precise and Ultrastable Orthogonal Nanoassembly. *J. Am. Chem. Soc.* **136**, 12355-12363. doi:10.1021/ja505584f

Gell, C., Bormuth, V., Brouhard, G. J., Cohen, D. N., Diez, S., Friel, C. T., Helenius, J., Nitzsche, B., Petzold, H., Ribbe, J. et al. (2010). Microtubule dynamics reconstituted in vitro and imaged by single-molecule fluorescence microscopy. In *Microtubules, in Vitro* (ed. L. Wilson and J. Correia), pp. 221-245. Academic Press.

Gennerich, A., Carter, A. P., Reck-Peterson, S. L. and Vale, R. D. (2007). Force-induced bidirectional stepping of cytoplasmic dynein. *Cell* **131**, 952-965. doi:10.1016/j.cell.2007.10.016

Grashoff, C., Hoffman, B. D., Brenner, M. D., Zhou, R., Parsons, M., Yang, M. T., McLean, M. A., Sligar, S. G., Chen, C. S., Ha, T. et al. (2010). Measuring mechanical tension across vinculin reveals regulation of focal adhesion dynamics. *Nature* **466**, 263-266. doi:10.1038/nature09198

Grishchuk, E. L., Molodtsov, M. I., Ataullakhanov, F. I. and McIntosh, J. R. (2005). Force production by disassembling microtubules. *Nature* **438**, 384-388. doi:10.1038/nature04132

Gudimchuk, N. B. and McIntosh, J. R. (2021). Regulation of microtubule dynamics, mechanics and function through the growing tip. *Nat. Rev. Mol. Cell Biol* **22**, 777-795. doi:10.1038/s41580-021-00399-x

Harasymiw, L. A., Tank, D., McClellan, M., Panigrahy, N. and Gardner, M. K. (2019). Centromere mechanical maturation during mammalian cell mitosis. *Nat. Commun* **10**, 1761. doi:10.1038/s41467-019-09578-z

Hirakawa, H., Ishikawa, S. and Nagamune, T. (2015). Ca2+-independent sortase-A exhibits high selective protein ligation activity in the cytoplasm of Escherichia coli. *Biotechnol. J* **10**, 1487-1492. doi:10.1002/biot.201500012

Honnappa, S., Gouveia, S. M., Weisbrich, A., Damberger, F. F., Bhavesh, N. S., Jawhari, H., Grigoriev, I., van Rijssel, F. J. A., Buey, R. M., Lawera, A. et al. (2009). An EB1-binding motif acts as a microtubule tip localization signal. *Cell* **138**, 366-376. doi:10.1016/j.cell.2009.04.065

Hua, B., Han, K. Y., Zhou, R., Kim, H., Shi, X., Abeysirigunawardena, S. C., Jain, A., Singh, D., Aggarwal, V., Woodson, S. A. et al. (2014). An improved surface passivation method for single-molecule studies. *Nat. Methods* **11**, 1233-1236. doi:10.1038/nmeth.3143

Huis in 't Veld, P. J., Jeganathan, S., Petrovic, A., Singh, P., John, J., Krenn, V., Weissmann, F., Bange, T. and Musacchio, A. (2016). Molecular basis of outer kinetochore assembly on CENP-T. *eLife* **5**, e21007. doi:10.7554/eLife.21007

Huis in 't Veld, P. J., Volkov, V. A., Stender, I. D., Musacchio, A. and Dogterom, M. (2019). Molecular determinants of the Ska-Ndc80 interaction and their influence on microtubule tracking and force-coupling. *eLife* **8**, e49539. doi:10.7554/eLife.49539

Iwaki, M., Wickham, S. F., Ikezaki, K., Yanagida, T. and Shih, W. M. (2016). A programmable DNA origami nanospring that reveals force-induced adjacent binding of myosin VI heads. *Nat. Commun* **7**, 13715. doi:10.1038/ncomms13715

Kuhn, J. and Dumont, S. (2019). Mammalian kinetochores count attached microtubules in a sensitive and switch-like manner. *J. Cell Biol* **218**, 3583-3596. doi:10.1083/jcb.201902105

Laan, L., Pavin, N., Husson, J., Romet-Lemonne, G., van Duijn, M., López, M. P., Vale, R. D., Jülicher, F., Reck-Peterson, S. L. and Dogterom, M. (2012). Cortical dynein controls microtubule dynamics to generate pulling forces that position microtubule asters. *Cell* **148**, 502-514. doi:10.1016/j.cell.2012.01.007

Lang, M. J., Fordyce, P. M., Engh, A. M., Neuman, K. C. and Block, S. M. (2004). Simultaneous, coincident optical trapping and single-molecule fluorescence. *Nat. Methods* **1**, 133-139. doi:10.1038/nmeth714

Lee, W. M., Reece, P. J., Marchington, R. F., Metzger, N. K. and Dholakia, K. (2007). Construction and calibration of an optical trap on a fluorescence optical microscope. *Nat. Protoc* **2**, 3226-3238. doi:10.1038/nprot.2007.446

Li, X. and Nicklas, R. B. (1995). Mitotic forces control a cell-cycle checkpoint. *Nature* **373**, 630-632. doi:10.1038/373630a0

Liu, D., Vader, G., Vromans, M. J. M., Lampson, M. A. and Lens, S. M. A. (2009). Sensing chromosome Bi-orientation by spatial separation of aurora B kinase from kinetochore substrates. *Science* **323**, 1350-1353. doi:10.1126/science.1167000

Long, A. F., Suresh, P. and Dumont, S. (2020). Individual kinetochore-fibers locally dissipate force to maintain robust mammalian spindle structure. *J. Cell Biol* **219**, e201911090. doi:10.1083/jcb.201911090

Miller, M. P., Asbury, C. L. and Biggins, S. (2016). A TOG protein confers tension sensitivity to kinetochore-microtubule attachments. *Cell* **165**, 1428-1439. doi:10.1016/j.cell.2016.04.030

Molodtsov, M. I., Mieck, C., Dobbelaere, J., Dammermann, A., Westermann, S. and Vaziri, A. (2016). A force-induced directional switch of a molecular motor enables parallel microtubule bundle formation. *Cell* **167**, 539-552.e14. doi:10.1016/j.cell.2016.09.029

Mukherjee, S., Sandri, B. J., Tank, D., McClellan, M., Harasymiw, L. A., Yang, Q., Parker, L. L. and Gardner, M. K. (2019). A gradient in metaphase tension leads to a scaled cellular response in mitosis. *Dev. Cell* **49**, 63-76.e10. doi:10.1016/j.devcel.2019.01.018

Musacchio, A. and Desai, A. (2017). A molecular view of kinetochore assembly and function. *Biology (Basel)* **6**, 5.

Neuert, G., Albrecht, C., Pamir, E. and Gaub, H. E. (2006). Dynamic force spectroscopy of the digoxigenin–antibody complex. *FEBS Lett.* **580**, 505-509. doi:10.1016/j.febslet.2005.12.052

Nicklas, R. B. (1983). Measurements of the force produced by the mitotic spindle in anaphase. *J. Cell Biol.* **97**, 542-548. doi:10.1083/jcb.97.2.542

Nicholas, M. P., Rao, L. and Gennerich, A. (2014). An improved optical tweezers assay for measuring the force generation of single kinesin molecules. In *Mitosis: Methods and Protocols* (ed. D. J. Sharp), pp. 171-246. New York, NY: Springer New York.

Pyrpassopoulos, S., Shuman, H. and Ostap, E. M. (2020). Modulation of Kinesin's load-bearing capacity by force geometry and the microtubule track. *Biophys. J* **118**, 243-253. doi:10.1016/j.bpj.2019.10.045

Rajendran, A., Endo, M., Katsuda, Y., Hidaka, K. and Sugiyama, H. (2011). Photo-cross-linking-assisted thermal stability of DNA origami structures and its application for higher-temperature self-assembly. *J. Am. Chem. Soc* **133**, 14488-14491. doi:10.1021/ja204546h

Ramakrishnan, S., Schärfen, L., Hunold, K., Fricke, S., Grundmeier, G., Schlierf, M., Keller, A. and Krainer, G. (2019). Enhancing the stability of DNA origami nanostructures: staple strand redesign versus enzymatic ligation. *Nanoscale* **11**, 16270-16276. doi:10.1039/C9NR04460D

Reck-Peterson, S. L., Yildiz, A., Carter, A. P., Gennerich, A., Zhang, N. and Vale, R. D. (2006). Single-molecule analysis of dynein processivity and stepping behavior. *Cell* **126**, 335-348. doi:10.1016/j.cell.2006.05.046

Rodríguez-García, R., Volkov, V. A., Chen, C.-Y., Katrukha, E. A., Olieric, N., Aher, A., Grigoriev, I., López, M. P., Steinmetz, M. O., Kapitein, L. C. et al. (2020). Mechanisms of motor-independent membrane remodeling driven by dynamic microtubules. *Curr. Biol.* **30**, 972-987.e12. doi:10.1016/j.cub.2020.01.036

Schindelin, J., Arganda-Carreras, I., Frise, E., Kaynig, V., Longair, M., Pietzsch, T., Preibisch, S., Rueden, C., Saalfeld, S., Schmid, B. et al. (2012). Fiji: an open-source platform for biological-image analysis. *Nat. Methods* **9**, 676-682. doi:10.1038/nmeth.2019

Suresh, P., Long, A. F. and Dumont, S. (2020). Microneedle manipulation of the mammalian spindle reveals specialized, short-lived reinforcement near chromosomes. *eLife* **9**, e53807. doi:10.7554/eLife.53807

Suzuki, A., Badger, B. L., Haase, J., Ohashi, T., Erickson, H. P., Salmon, E. D. and Bloom, K. (2016). How the kinetochore couples microtubule force and centromere stretch to move chromosomes. *Nat. Cell Biol.* **18**, 382-392. doi:10.1038/ncb3323

Thomas, G., Massimo, K., Benjamin, K. and Hendrik, D. (2022). Sequence-programmable covalent bonding of designed DNA assemblies. *Sci. Adv* **4**, eaau1157.

Tinberg, C. E., Khare, S. D., Dou, J., Doyle, L., Nelson, J. W., Schena, A., Jankowski, W., Kalodimos, C. G., Johnsson, K., Stoddard, B. L. et al. (2013). Computational design of ligand-binding proteins with high affinity and selectivity. *Nature* **501**, 212-216. doi:10.1038/nature12443

Tokunaga, M., Imamoto, N. and Sakata-Sogawa, K. (2008). Highly inclined thin illumination enables clear single-molecule imaging in cells. *Nat. Methods* **5**, 159-161. doi:10.1038/nmeth1171

Van Patten, W. J., Walder, R., Adhikari, A., Okoniewski, S. R., Ravichandran, R., Tinberg, C. E., Baker, D. and Perkins, T. T. (2018). Improved free-energy landscape quantification illustrated with a computationally designed protein–ligand interaction. *Chemphyschem* **19**, 19-23. doi:10.1002/cphc.201701147

Volkov, V. A. (2020). Microtubules pull the strings: disordered sequences as efficient couplers of microtubule-generated force. *Essays Biochem.* **64**, 371-382. doi:10.1042/EBC20190078

Volkov, V. A., Zaytsev, A. V., Gudimchuk, N., Grissom, P. M., Gintsburg, A. L., Ataullakhanov, F. I., McIntosh, J. R. and Grishchuk, E. L. (2013). Long tethers provide high-force coupling of the Dam1 ring to shortening microtubules. *Proc. Natl. Acad. Sci. USA* **110**, 7708-7713.

Volkov, V. A., Zaytsev, A. V. and Grishchuk, E. L. (2014). Preparation of segmented microtubules to study motions driven by the disassembling microtubule ends. *J. Vis. Exp.* **85**, e51150. doi:10.3791/51150.

Volkov, V. A., Huis in 't Veld, P. J., Dogterom, M. and Musacchio, A. (2018). Multivalency of NDC80 in the outer kinetochore is essential to track shortening microtubules and generate forces. *eLife* **7**, e36764. doi:10.7554/eLife.36764

Ye, A. A., Cane, S. and Maresca, T. J. (2016). Chromosome biorientation produces hundreds of piconewtons at a metazoan kinetochore. *Nat. Commun* **7**, 13221. doi:10.1038/ncomms13221

Yoo, T. Y., Choi, J.-M., Conway, W., Yu, C.-H., Pappu, R. V. and Needleman, D. J. (2018). Measuring NDC80 binding reveals the molecular basis of tension-dependent kinetochore-microtubule attachments. *eLife* **7**, e36392. doi:10.7554/eLife.36392